



## Topological phase detection through high-harmonic spectroscopy in extended Su-Schrieffer-Heeger chains

Mohit Lal Bera,<sup>1</sup> Jessica O. de Almeida<sup>1</sup>, Marlena Dziurawiec,<sup>2</sup> Marcin Płodzień,<sup>1</sup> Maciej M. Maśka<sup>2</sup>, Maciej Lewenstein,<sup>1,3</sup> Tobias Grass,<sup>4,5,1</sup> and Utso Bhattacharya<sup>1</sup>

<sup>1</sup>*ICFO - Institut de Ciències Fotòniques, The Barcelona Institute of Science and Technology, 08860 Castelldefels (Barcelona), Spain*

<sup>2</sup>*Institute of Theoretical Physics, Wrocław University of Science and Technology, 50-370 Wrocław, Poland*

<sup>3</sup>*ICREA, Pg. Lluis Companys 23, ES-08010 Barcelona, Spain*

<sup>4</sup>*DIPC - Donostia International Physics Center, Paseo Manuel de Lardizábal 4, 20018 San Sebastián, Spain*

<sup>5</sup>*Ikerbasque - Basque Foundation for Science, Maria Diaz de Haro 3, 48013 Bilbao, Spain*



(Received 14 June 2023; accepted 27 November 2023; published 14 December 2023)

Su-Schrieffer-Heeger (SSH) chains are paradigmatic examples of one-dimensional topological insulators hosting zero-energy edge modes when the bulk of the system has a nonzero topological winding invariant. Recently, high-harmonic spectroscopy has been suggested as a tool for detecting the topological phase. Specifically, it has been shown that when the SSH chain is coupled to an external laser field of a frequency much smaller than the band gap, the emitted light at harmonic frequencies strongly differs between the trivial and the topological phase. However, it remains unclear whether various nontrivial topological phases—differing in the number of edge states—can also be distinguished by the high-harmonic generation (HHG). In this paper, we investigate this problem by studying an extended version of the SSH chain with extended-range hoppings, resulting in a topological model with different topological phases. We explicitly show that HHG spectra are a sensitive and suitable tool for distinguishing topological phases when there is more than one topological phase. We also propose a quantitative scheme based on tuning the filling of the system to precisely locate the number of edge modes in each topological phase of this chain.

DOI: [10.1103/PhysRevB.108.214104](https://doi.org/10.1103/PhysRevB.108.214104)

### I. INTRODUCTION

In recent years, the field of condensed matter physics has seen an increasing interest in the study of topological phases of matter. These phases are characterized by nonlocal and nonperturbative properties that are protected by topological invariants, which are robust against perturbations and imperfections. The discovery of topological insulators [1–5] and topological superconductors [6,7] has led to the exploration of a wide range of topological phases in different materials, including cold atoms [8] and photonic [9–11] systems. The study of these systems is not only of fundamental interest but also has potential applications in various fields, such as quantum computing [12–15], spintronics [16], and magnetometry [17]. The Su-Schrieffer-Heeger (SSH) model is one of the simplest models that exhibits nontrivial topological properties. It is a one-dimensional model originally introduced to describe the electronic properties of polyacetylene [18,19], a linear polymer of carbon and hydrogen atoms. The model is described by a tight-binding Hamiltonian representing the hopping of electrons between adjacent sites, with two different parameters representing alternating single and double bonds. The SSH model exhibits two different phases, characterized by the number of edge states that appear in the band gap at zero energy. In the trivial phase, there are no zero-energy states, whereas, in the topological phase, there are two such states that appear at the open ends of the system. Various extensions of the SSH model have been explored, including longer-range tunneling terms that describe the hopping

between second nearest neighbors [15,20,21]. An appropriately extended SSH model may exhibit additional topological phases, such as a phase characterized by four edge states.

Recent advancements have demonstrated that the ESSH model can now be replicated in real materials or molecules in laboratories. Notably, the SSH model has been associated with certain graphene nanoribbons [22]. There are also other platforms experimentally available that can represent the SSH model or its extended variations. Some notable instances are *p*-orbit optical ladder systems [23] and bichromatic optical lattices with off-diagonal configurations [24]. It is important to emphasize that even if our particular model has not been directly simulated experimentally, ultracold atoms within momentum lattices have successfully captured an extended variant of the SSH model. This version closely mirrors the model we have elaborated on in our research [25]. Given these findings, systems resembling graphene nanoribbons, whether influenced by Floquet dynamics or not, or systems with similar characteristics, might very well accommodate the extended SSH models we have investigated in our study.

High-harmonic spectroscopy in condensed matter is a burgeoning field in strong-field attosecond science that has the potential to uncover the structural and dynamical properties of materials [26,27]. High-harmonic generation (HHG) is a nonlinear optical process that occurs when an intense laser field interacts with a material, producing high-order harmonics of the incident frequency. In recent years, the connection between strong-field attosecond science and topological condensed matter has started to be explored theoretically [28–36]

and experimentally [37,38]. Despite the lack of success in finding universal signatures of topology in the high-harmonic spectroscopy of quantum spin-Hall materials [39], a few signatures of topology have been explored in analyzing the polarization of the emitted harmonics and the Stokes parameters [40]. In models with strong electronic interaction, the effect of doping in high-harmonic spectroscopy has been analyzed [41].

In the context of the SSH model, theoretical studies have shown that high-harmonic spectroscopy can be used to detect topological properties [29,30]. In particular, the high-harmonic spectra of the SSH model exhibit characteristic features that allow one to distinguish between trivial and nontrivial topological phases and to identify the topological edge states. Nevertheless, it remains unclear whether two different nontrivial topological phases, with various nonzero numbers of edge states, can also be identified using HHG.

To address this issue, in this paper, we consider the extended version of the SSH model, which includes second-neighbor electronic hopping as studied in Ref. [21]. This model exhibits topological phases with zero, two, and four-edge states. We propose a method to distinguish between these phases using high-harmonic spectroscopy. Our method is based on the analysis of the nonlinear polarization of the material, which reveals characteristic signatures of the topological phases. We show that our method can provide a clear distinction between materials with two- and four-edge states and it can be used to identify and control the topological properties of other topological materials. Our method could have significant implications for the study of topological phases in condensed matter and could aid in the development of new technologies.

The paper has the following structure. In Sec. II, within subsection II A, we introduce the extended SSH model and discuss its band structure, topological properties, and phase diagram in comparison with the standard SSH model. In subsection II B, we provide specific details about the induced laser pulse and the coupling of light to the extended SSH chain. In subsection II C we shortly describe the numerical technique required to calculate the high-harmonic spectrum for three different phases of the system. In Sec. III we discuss the high-harmonic spectra obtained for three different phases and investigate the role of filling in accurately determining the number of edge modes in each of the three phases of the system. Finally, we summarize our work in the concluding Sec. IV with a brief outlook and experimental possibilities.

## II. THEORY

### A. Extended Su-Schrieffer-Heeger model

The Su-Schrieffer-Heeger (SSH) model [42,43] is a theoretical model used in solid-state physics to describe the electronic properties of one-dimensional crystalline systems. The model considers a chain of alternating atoms in sublattices A and B in a two-site unit cell [30]. The electrons hop inside the unit cell (intracell) and between nearest-neighbor unit cells (intercells) with different hopping amplitudes. The model is thus characterized by a parameter called the dimerization parameter, which represents the difference in the

hopping strengths between the intra- and intercellular bonds. When the intercellular dimerization is stronger than the intracellular one, it exhibits a nontrivial topological phase with a bulk gap and supports the presence of topologically protected edge states at the boundary of the chain. This allows the SSH model to be a prototypical model of a one-dimensional (1D) topological insulator. The topological nature of the SSH model is due to the presence of a chiral symmetry, which is a discrete symmetry that anticommutes with the SSH Hamiltonian and shows that the model is invariant under the exchange of its two sublattices. It also ensures that, for every positive energy of the system, there exists a negative energy with the same magnitude. Interestingly, the energies are also symmetric under swap of the dimerizations and the dispersion relation is identical and gapped everywhere (insulator), except when the dimerization is zero, where it is gapless (metal). However, the system has distinct properties under swap of the dimerization as the eigenvectors differ significantly. In fact, when the Berry curvature of the eigenvectors in quasimomentum space is integrated over the entire Brillouin zone, one finds different topological invariants called Chern numbers [44]. This shows that the two insulating phases are topologically distinct. Different topological sectors imply the impossibility of crossing from an insulating phase to another without undergoing a topological phase transition, which involves the closing of the bulk gap (i.e., the metallic phase where the winding number is ill defined) of the system. This is why when the system with a nonzero bulk topological invariant is put under an open boundary condition, there appears a zero-energy (edge) mode within the bulk gap of the system, sharply localized at the boundary separating a topologically nontrivial region (insulator) from a topologically trivial one. The noninteracting tight-binding model used in this study does not consider electron-electron interactions. As a result, it is possible to obtain precise analytical results for both the band structure and the winding number, making it a representative example of a 1D topological insulator [2]. So far, the SSH model has been experimentally realized in various systems: cold atoms [45], photonic lattices [46,47], and mechanical systems [48].

The topological phase diagram of the standard SSH can be extended to include phases with higher values of topological invariants if not restricted to only nearest-neighbor electronic hopping. Allowing for a longer range of hopping, such as hopping between second-neighbor sites, generates a model, which we denote as an extended Su-Schrieffer-Heeger (ESSH) model, extensively studied in Ref. [21]. However, hoppings only between the different sublattices are included to preserve the chiral symmetry of the model, which in turn keeps the topology intact. More specifically, in this work, we study the Hamiltonian of the 1D ESSH model:

$$\begin{aligned} \mathcal{H} = & J_1 \sum_{n=1}^N (\hat{c}_{n,A}^\dagger \hat{c}_{n,B} + \text{H.c.}) + J'_1 \sum_{n=1}^N (\hat{c}_{n,B}^\dagger \hat{c}_{n+1,A} + \text{H.c.}) \\ & + J_3 \sum_{n=1}^N (\hat{c}_{n,A}^\dagger \hat{c}_{n+1,B} + \text{H.c.}) + J'_3 \sum_{n=1}^N (\hat{c}_{n,B}^\dagger \hat{c}_{n+2,A} + \text{H.c.}), \end{aligned} \quad (1)$$

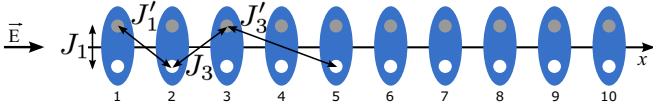


FIG. 1. Schematic representation of the one-dimensional ESSH model described by the Hamiltonian [Eq. (2)]. Each blue ellipse represents a unit cell containing two sites:  $A$ -type sites drawn below and  $B$ -type sites drawn above. To keep chiral symmetry intact, we only include hopping processes between  $A$ -type and  $B$ -type sites, including intracell hopping  $J_1$ , hoppings between neighboring cells  $J_3$  and  $J'_3$ , as well as hopping between next-to-nearest cells  $J'_3$ .

where  $N$  is the number of cells in a chain of  $M = 2N$  sites in the chain. In the second quantized notation,  $\hat{c}_{n,s}^\dagger$  ( $c_{n,s}$ ) is the electron creation (annihilation) operator in the unit cell  $n$  with sublattices  $s = A, B$ . The first term represents intracellular electron hopping with strength  $J_1$ , the second represents the nearest-neighbor intercellular hopping between  $B$  in cell  $n$  and  $A$  in cell  $n + 1$ , and the third is the nearest-neighbor hopping between  $A$  in cell  $n$  and  $B$  in cell  $n + 1$ , while the fourth term captures the next nearest-neighbor hopping between  $B$  in cell  $n$  and  $A$  in cell  $n + 2$  (see Fig. 1). In the first quantized notation, the Hamiltonian in real space can be written as

$$\begin{aligned} \mathcal{H} = & J_1 \left( \sum_{n=1}^N |n, A\rangle \langle n, B| + \text{H.c.} \right) \\ & + J'_1 \left( \sum_{n=1}^N |n, B\rangle \langle n+1, A| + \text{H.c.} \right) \\ & + J_3 \left( \sum_{n=1}^N |n, A\rangle \langle n+1, B| + \text{H.c.} \right) \\ & + J'_3 \left( \sum_{n=1}^N |n, B\rangle \langle n+2, A| + \text{H.c.} \right). \end{aligned} \quad (2)$$

As in the standard SSH model, the extended SSH model Hamiltonian also preserves the three discrete symmetries, chiral, particle hole, and time reversal, and is classified under the BDI topological class with its topological invariant (the winding number) belonging to the set of integers  $\mathbb{Z}$ . On an open boundary, the ESSH can host different numbers of edge modes: zero, two, or four edge modes, depending on the absolute value of its bulk winding number being zero, one, or two. In contrast, the standard SSH model possesses only two possibilities—zero or two edge modes on the ends of the open chain.

It is straightforward to calculate the winding number by writing down the Hamiltonian in Eq. (2) in momentum representation, which can be obtained by replacing

$$\begin{aligned} |n, A\rangle &= \sum_k e^{-ikx_{nA}} |k, A\rangle, \\ |n, B\rangle &= \sum_k e^{-ik'x_{nB}} |k', B\rangle, \end{aligned} \quad (3)$$

where  $k$  index is associated with sublattice  $A$  and  $k'$  index is associated with sublattice  $B$ ;  $|k, s\rangle$  is the quasimomentum ket with momentum  $k$  using periodic boundary conditions. In the

rest of the work, we denote the lattice size constant of  $a$ . With this, the Hamiltonian in Eq. (2) reduces to

$$\mathcal{H} = \sum_k (|k, A\rangle, |k, B\rangle) [h_x(k)\sigma_x + h_y(k)\sigma_y] \begin{pmatrix} \langle k, A| \\ \langle k, B| \end{pmatrix}, \quad (4)$$

where

$$\begin{aligned} h_x(k) &= J_1 + J'_1 \cos ka + J_3 \cos ka + J'_3 \cos 2ka, \\ h_y(k) &= J'_1 \sin ka - J_3 \sin ka + J'_3 \sin 2ka. \end{aligned} \quad (5)$$

Due to the presence of discrete translational invariance in the system, it is reduced to two-level systems in the sublattice basis for each quasimomentum mode  $k$  and can therefore be easily written down in terms of Pauli matrices  $\sigma_x$  and  $\sigma_y$ . Furthermore, this decomposition into the Pauli basis allows us to compute the winding number using  $h_x$  and  $h_y$ ,

$$\mathcal{W} = \frac{1}{2\pi} \int_{\text{BZ}} \frac{h_x \partial_k h_y - h_y \partial_k h_x}{h_x^2 + h_y^2} dk. \quad (6)$$

The winding number for this model can have values  $\mathcal{W} = -1, 0, 1, 2$ , which through the bulk-boundary correspondence directly yields the number of edge modes the system possesses in an open boundary condition as two times its absolute value  $2|\mathcal{W}|$ . From the energy spectrum plotted in Fig. 2, one can see the band gap structure, the different number of zero energy modes or edge modes, and the winding number for the two most interesting cases when the system (a) has winding number one and thus one pair of edge modes and (b) has two pairs of edge modes with winding number two. Fixing the value of the parameters  $J_1 = J'_1 = 1$ , one can vary the other two parameters  $J_3$  and  $J'_3$  and calculate the winding number to obtain a phase diagram showing different possible phases in the ESSH system, as illustrated in Fig. 3.

## B. Incident laser field

In this section, we study the coupling of the 1D ESSH model to a linearly polarized electric field from a laser. The laser wavelength is assumed to be much larger than the length of the system and, as such, the coupling to the laser field is well captured within the dipole approximation. The laser vector potential and electric field are

$$\vec{A}(t) = A(t)\hat{x}, \quad \vec{E}(t) = -\partial_t \vec{A}(t), \quad (7)$$

where  $\hat{x}$  is the direction along the length of the chain parallel to the laser polarization. The way in which the light couples to the matter depends on the geometry of the system. For instance, in the velocity gauge, the light-matter coupling provides the hopping elements with Peierls' phases  $\vec{A} \cdot (\vec{r}_{n,s} - \vec{r}_{n',s'})$ . For concreteness, we assume that  $\vec{A} \cdot (\vec{r}_{n,s} - \vec{r}_{n',s'}) \propto n - n'$ . Therefore, the intracell hopping remains unaffected by the light, i.e.,  $\vec{A} \cdot (\vec{r}_{n,A} - \vec{r}_{n,B}) = 0$ , whereas hopping between neighboring cells acquires a phase  $A(t)$  and hopping between next-to-nearest cells a phase  $2A(t)$ . Accordingly, we have

$$\begin{aligned} J_1(t) &= J_1, & J'_1(t) &= J'_1 e^{iaA(t)}, \\ J_3(t) &= J_3 e^{iaA(t)}, & J'_3(t) &= J'_3 e^{2iaA(t)}. \end{aligned} \quad (8)$$

The eigenstates of the  $N \times N$ -dimensional ESSH Hamiltonian (1) are obtained by exact diagonalization in a

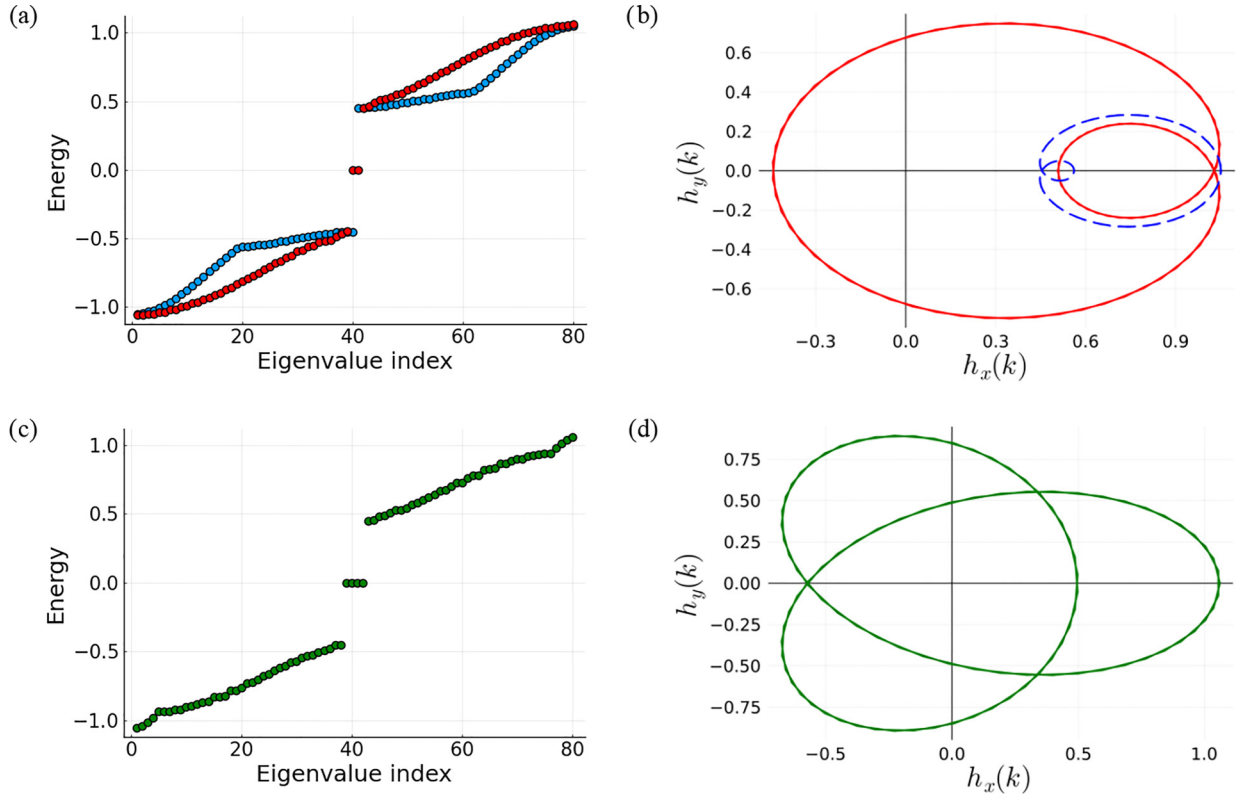


FIG. 2. Energy eigenvalues with 80 sites (in a.u.), showing zero [(a), blue], two [(a), red], and four [(c), green] zero-energy states with different fixed parameter values of the Hamiltonian [Eq. (2)]. The figures on the right show the parametric plot of  $h_x(k)$  and  $h_y(k)$  as defined in Eq. (4), with two (b) and four (d) zero energy states. The parameters used to generate the figures are as follows: for absence of zero-energy states  $J_1 = 0.651$ ,  $J'_1 = 0.207$ ,  $J_3 = 0.038$ , and  $J'_3 = 0.156$ ; for two zero-energy states  $J_1 = 0.51$ ,  $J'_1 = 0.42$ ,  $J_3 = 0.056$ , and  $J'_3 = -0.479$ ; for four zero-energy states  $J_1 = 0.059$ ,  $J'_1 = 0.021$ ,  $J_3 = 0.26$ , and  $J'_3 = 0.7209$ .

real space single particle basis. The  $N/2$  lowest energy states (occupied by  $N$  electrons, assuming spin degeneracy) are time evolved within the whole laser pulse duration consisting of 5 cycles ( $n_c = 5$ ). Assuming atomic units ( $\hbar = |e| = m_e = 4\pi\epsilon_0 = 1$ ), the incident laser field has the

shape

$$A(t) = A_0 \sin^2\left(\frac{\omega t}{2n_c}\right) \sin(\omega t), \quad 0 < t < \frac{2\pi n_c}{\omega}. \quad (9)$$

The frequency is set to  $\omega = 0.03$  a.u. (corresponding to  $\lambda \simeq 1.5 \mu\text{m}$  and pulse duration  $\tau \simeq 25$  fs), and the vector potential amplitude is  $A_0 = 0.5$  (corresponding to a laser intensity  $\simeq 20 \times 10^{10} \text{ W cm}^{-2}$ ) throughout the paper. The results which we discuss in this paper do not depend on the details of the laser pulse as long as the incident laser frequency is small compared to the band gap in the insulating phases and the peak strength of the laser is large enough to generate high harmonics.

The evolution of the wave function with the time-dependent Hamiltonian was calculated using the Crank-Nicolson approximation,

$$\begin{aligned} |\Psi(t + \delta t)\rangle &= \exp[-i\mathcal{H}(t)\delta t]|\Psi(t)\rangle \\ &\approx \frac{1 - i\mathcal{H}(t + \delta t/2)\delta t/2}{1 + i\mathcal{H}(t + \delta t/2)\delta t/2}|\Psi(t)\rangle, \end{aligned} \quad (10)$$

solved in individual infinitesimal  $\delta t$  time steps, with the initial condition  $|\Psi(0)\rangle$  being the ground state of the system. The numerical results in this paper result from time evolving the wave function in  $2\pi n_c/\omega$  steps.

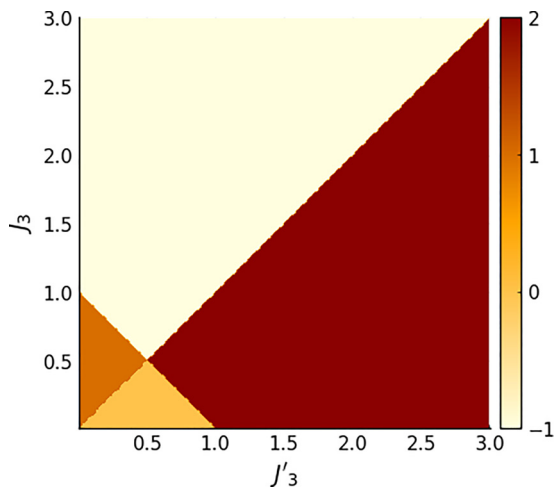


FIG. 3. Topological phase diagram of the Hamiltonian [Eq. (4)] showing various values of the winding number for fixed  $J_1 = J'_1$  varying  $J_3$  and  $J'_3$  (in units of  $J_1$ ), calculated as in Eq. (6).



### C. High-harmonic generation

Our primary goal is to estimate the high-harmonic spectrum of the ESSH system. Within the semiclassical approach, for uncorrelated emitters, the spectrum of the radiated light is proportional to the absolute square of the Fourier transform of the dipole acceleration [49–51],

$$P(\omega) = |\text{FFT}[W_B \ddot{X}(t)]|^2, \quad (11)$$

where  $\ddot{X}(t)$  is the acceleration or the double time derivative of the time-dependent position operator and  $W_B$  is the Blackman window function [52]. This window function avoids excitation at high frequencies and abrupt transitions in the spectra, highlighting the effects below the band gap. To calculate the time-dependent expectation value of the position operator, we time evolve all occupied eigenstates  $b$ ,  $b \in (1, N/2)$ . The time-evolved single-particle wave function  $\Psi_b(t)$  is then used to compute

$$X(t) = \sum_{b=1}^{N/2} \sum_{j=1}^N \sum_{s=A,B} \Psi_b^{j,s*}(t) x_{j,s} \Psi_b^{j,s}(t), \quad (12)$$

where  $\Psi_b^{j,s}(t)$  is the amplitude of the time evolved wave function on site  $s$  of cell  $j$  and the position  $x_{j,s}$  is given by

$$x_{j,A} = x_{j,B} = (j-1) - \frac{(a-M)}{4}, \quad (13)$$

where  $j$  is the position of each cell with two sites  $A$  and  $B$ , as shown in Fig. 1. Essentially, the time-evolved average positions of all electrons in different (initial) filled eigenstates are summed to obtain the total position of the electron cloud.

In the next section, we analyze and compare the time-dependent position and the harmonic response of the system at three different parameter points, corresponding to three different phases as illustrated in Fig. 2, as follows. (a) Phase  $P_0$ , represented by the parameter point  $J_1 = 0.651$ ,  $J'_1 = 0.207$ ,  $J_3 = 0.038$ , and  $J'_3 = 0.156$ . From the energy spectrum presented in Fig. 2(a) (blue), we observe the energy band gap of 0.9 (in atomic units) and the winding number of  $\mathcal{W} = 0$  corresponding to the trivial insulator phase. (b) Phase  $P_1$ , represented by the point  $J_1 = 0.51$ ,  $J'_1 = 0.42$ ,  $J_3 = 0.056$ , and  $J'_3 = -0.479$ . It is illustrated in Fig. 2(a) (red), exhibiting the presence of two zero-energy states that indicate the edge states, in agreement with the winding number  $\mathcal{W} = 1$ . (c) Phase  $P_2$ , represented by  $J_1 = 0.059$ ,  $J'_1 = 0.021$ ,  $J_3 = 0.26$ , and  $J'_3 = 0.7209$ . For this phase, we observe in Fig. 2(b) the presence of four zero-energy states, representing the edge modes with  $\mathcal{W} = 2$ . The parameter choices have been made such that the system has the same band gap and bandwidth in all three phases, allowing for a clear comparison of the results amongst all three phases. We also look at the phase transition point  $M$ , which is a metal with the parameters  $J_1 = 0.51$ ,  $J'_1 = 0.42$ ,  $J_3 = 1$ , and  $J'_3 = 0.91$ . The overall goal is to observe whether, through the time-dependent position operator and the harmonic spectra, one can identify certain signatures, which will enable a clear distinction between  $P_0$ ,  $P_1$ ,  $P_2$ , and  $M$ .

## III. RESULTS AND DISCUSSIONS

We first look at the expectation value of the total position operator of the ESSH model as a function of time, as

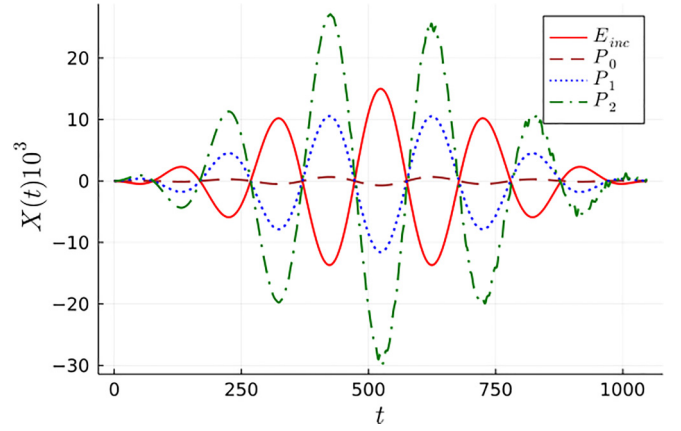


FIG. 4. Incident electric field (red, solid line) and the expected value of the position operator [Eq. (12)] as a function of time for different topological phases  $P_0$ ,  $P_1$ , and  $P_2$ .

illustrated in Fig. 4 for the three different phases  $P_0$ ,  $P_1$ , and  $P_2$ . The position operator has a similar periodicity in all the phases as that of the incident laser beam [Eq. (9)], but there is a clear difference in the maximum amplitude for the three phases. Apparently, the change in the average electronic position is the lowest in the topologically trivial insulating phase  $P_0$  and can be attributed to the overall localized nature of the electronic cloud for a half-filled insulator. The presence of edge modes makes the system slightly more metallic and hence the displacement is more in phases ( $P_1$ ,  $P_2$ ) with more edge modes in the system. This becomes more apparent as one studies the harmonic spectra of the system.

As shown in Fig. 4, the expected value of the position operator is consistently synchronized with the incident field with a  $\pi/2$  phase shift. Similarly, the expected value of the current operator [53] for the ESSH model shows the same behavior. This is a consequence of the insulating nature of the ESSH bulk.

In Fig. 5, we plot the logarithm of the absolute power spectra of the harmonic spectra versus the harmonic order (integer multiple of the incident driving frequency). The harmonic spectra for  $P_0$ ,  $P_1$ , and  $P_2$  show a plateau at high energies beyond the band gap of the system. The plateau arises mainly from interference between electronic trajectories that undergo interband transitions. A cutoff is also observed at similar harmonic order for all three curves, as it is primarily determined by the bandwidth (energy difference between highest and lowest eigenenergy) of the system, which limits the maximum energy that the electrons can attain during evolution. However, the harmonic response below the band gap is different for the  $P_0$  and  $P_1$ ,  $P_2$  phases. This region, which in usual semiconductors is mainly dominated by intraband contributions, has a dip for  $P_0$ . However, in phases  $P_1$  and  $P_2$ , we do not observe a dip below the band gap, because midband gap states are available for electronic transition due to edge modes. These appear as clear signals in the harmonic spectra as now transitions between the filled bulk bands to the midgap edge states are possible. In contrast, the  $P_0$  phase is a trivial insulator with a bulk gap and no midgap states and thus the bulk states can

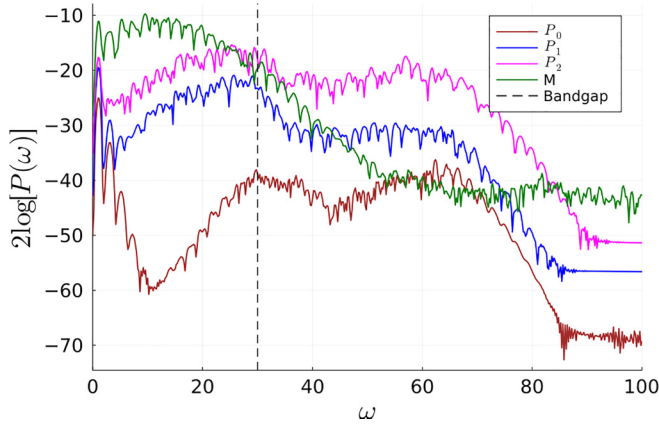


FIG. 5. High-harmonic spectra emitted for the phases: metallic  $M$ , topologically trivial  $P_0$ , and two different topologically nontrivial  $P_1$  (with two edge modes) and  $P_2$  (with four edge modes). The vertical line corresponds to the value of the band gap (in the units of the incident laser frequency).

only contribute to the harmonic spectra beyond the band gap. Consequently, there occurs a dip in the signal below the band gap for such a phase. This feature that allows one to distinguish between the high-harmonic spectra of topologically trivial and nontrivial phases was also observed in previous studies of the HHG in the SSH model [29,30]. Moreover, it has been studied in topological superconductors and the topological nature of the edge modes has been confirmed by showing that it is robust under local perturbations via the HHG [36].

However, interestingly, it is not easy to distinguish between the two topological phases based on the harmonic spectra itself, as the overall amplitude difference in the time-dependent position being polynomial does not appear as a big difference in the harmonic spectra, which is plotted on a logarithmic scale and depends on the specific values of the hopping parameters chosen for these two phases. Despite this, by analyzing the contributions of both bulk and edge states to the high harmonics and using the harmonic spectra of the trivial insulating phase  $P_0$  and the metallic phase transition point  $M$  as two extreme reference limits to test for metallicity, we can elaborate below how precise control over the electronic filling in the ESSH chain allows us to clearly distinguish between all the different topological phases based solely on the HHG spectra.

We assume an ESSH chain away from half filling where the number of electrons in the chain is  $\nu$  less than  $N/2$ . Then the expectation value of the position operator is given by

$$X(t, \nu) = \sum_{b=1}^{N/2-\nu} \sum_{j=1}^N \sum_{s=A,B} \Psi_b^{j,s*}(t) x_{j,s} \Psi_b^{j,s}(t). \quad (14)$$

As a consequence, varying the ESSH chain filling, i.e., changing the value of  $\nu = \{0, 1, 2, 3, 4\}$ , affects the HHG spectra [Eq. (11)] of phases  $P_0$ ,  $P_1$ , and  $P_2$  as shown in Fig. 6.

We first focus on phase  $P_0$  [see Fig. 2(a)] and compare the HHG spectra for various fillings against the one at exactly half filling (yellow). It can be clearly observed that, for filling values up to  $N/2 - 1$ , the HHG spectra are almost identical regardless of the filling. In fact, away from half filling, the

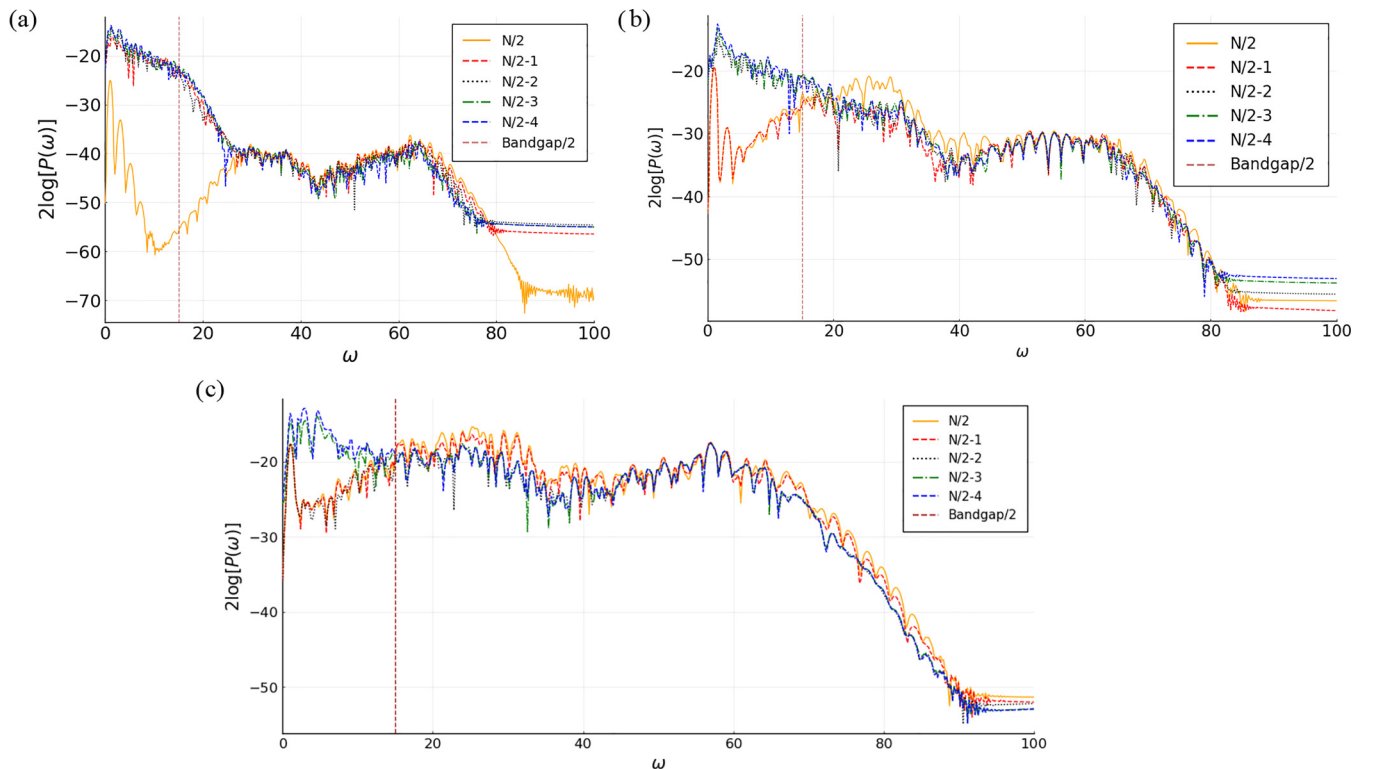


FIG. 6. High-harmonic spectra for different phases. (a) Phase  $P_0$  (zero edge modes). (b) Phase  $P_1$  (two edge modes). (c) Phase  $P_2$  (four edge modes). Different colors correspond to various fillings of the system. The vertical line indicates half of the value of the band gap (in units of the incident laser frequency).

spectra have no dips at half the band gap. This is because, even slightly away from half filling, the system is no longer an insulator and there are a small number of states available (depending on the filling) for transition within the bulk states below the band gap, producing significant HHG spectra from intraband dynamics within this partially filled valence band. These HHG spectra resemble those of a metal, as can be seen by comparison with the green curve in Fig. 5. The order-of-magnitude difference (in logarithmic scale) between the spectra at half filling and the one away shows how sensitive the probe of the HHG spectra is to the filling of the system that produces metallicity and that does not.

This sensitivity acts as a means of quantitatively distinguishing the presence of the number of edge modes in phases  $P_1$  [see Fig. 2(b)] and  $P_2$  [see Fig. 2(c)]. By varying the filling of the system with parameters from the  $P_1$  ( $P_2$ ) phase, we see that the system shows a metallic HHG spectra until  $N/2 - 2$  ( $N/2 - 3$ ) states are filled; then suddenly it shows a dip as the bulk of the system becomes insulating when  $N/2 - 1$  ( $N/2 - 2$ ) states are filled. Thus, by continuously monitoring the filling, it is possible to count how many states ahead of half filling the system shows a transition from metallic to insulating behavior. This difference in the number of states gives the number of pairs of edge modes in the system.

The dip in the harmonic power spectra at the filling, where the transition from bulk metallic to bulk insulating behavior occurs, can be quantitatively determined by summing the inverse of the squared value of power spectra below half the band gap for every value of  $\nu$  as

$$S_p(\nu) = \sum_{w=0}^{\Delta E/2} \frac{1}{P(\omega, \nu)^2}, \quad (15)$$

where  $\Delta E$  is the bulk band gap energy of the system (edge modes excluded). The sum is taken over half the band gap; as expected, the sharp change only affects the harmonic modes below the band gap in the harmonic spectra.

The transition shows up in this quantity  $S_p(\nu)$  as a sharp jump with at least ten orders of magnitude difference. In phase  $P_0$ , the transition occurs between the completely filled,  $\nu = 0$ , to  $\nu = 1$ , where  $S_p(0) \sim 10S_p(1)$  says that the number of pairs of edge modes in the system is zero. In phase  $P_1$ , the transition takes place between  $\nu = 1$  and  $\nu = 2$ , where  $S_p(0) \sim S_p(1) \sim 10S_p(2)$  and then the system possesses just one pair of edge modes. In phase  $P_2$ , the transition is from  $\nu = 2$  to  $\nu = 3$ , which changes  $S_p(\nu)$  as  $S_p(0) \sim S_p(1) \sim S_p(2) \sim 10S_p(3)$ , correctly indicating that there are two pairs of edge modes in the system. We show an illustrative plot of this behavior in Fig. 7.

#### IV. CONCLUSIONS

In summary, in this work, we allow for second-nearest-neighbor hopping in addition to the nearest-neighbor hopping already present in the standard SSH model, with hopping terms within a sublattice being forbidden. This creates the ESSH model with the chiral symmetry in the SSH model being preserved. However, this expands the topological phase diagram of the SSH model to now include new topological phases with higher winding numbers. Such a system under

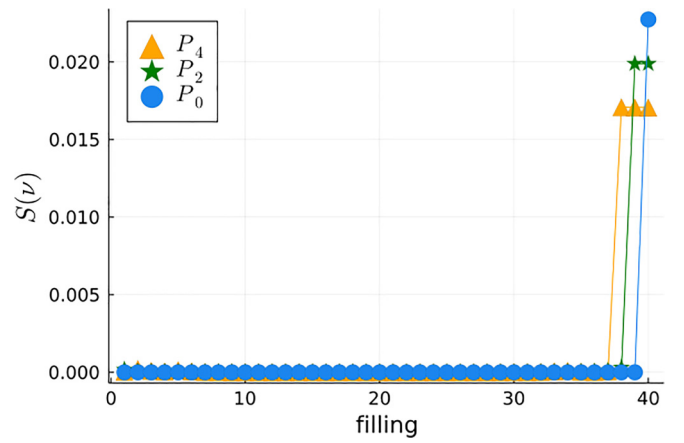


FIG. 7.  $S_p(\nu)$  versus filling for different phases  $P_0$ ,  $P_2$ , and  $P_4$ . It shows a peak when all the states in the bulk are filled and the edge states start to be filled. One state in the peak represents zero edge modes or phase  $P_0$  [ $S_{P_0}(\nu) \sim 10^9 S_{P_4}(\nu)$ ], two states in the peak represent two edge modes or phase  $P_2$  [ $S_{P_2}(\nu) \sim 10^7 S_{P_4}(\nu)$ ], and three states in the peak represent four edge modes or phase  $P_4$ .

an open boundary condition has three insulating phases with zero, two, and four edge modes at each end of the chain.

We shine a five-cycle ultrafast laser pulse with strong intensities and below the bulk band gap frequencies parallel to the length of the ESSH chain and calculate the emitted harmonic spectra in response to this illumination. The harmonic spectra in the linear scale shows that the overall below-the-band gap response of the system is different for its three phases, with the amplitude being higher when the system has more edge modes. However, although the distinction is clearly visible between the HHG spectra from the trivially insulating versus the topological ones, the distinction between the two topological phases is hard to perceive in the logarithmic scale. Therefore, we did a careful analysis of the HHG spectra as a function of filling to show that the HHG spectra are very sensitive to the change from bulk insulating behavior to bulk metallic behavior, as filling is continuously varied. Therefore, tracking where the bulk insulating behavior sets in, as a function of filling, we manage to count off the number of pairs of edge states in the system. We have also proposed a quantity that can sharply detect this transition.

Our work concentrates on studying an idealized model which features different topological phases. Our goal was to investigate whether and how HHG is suitable for distinguishing between these phases. Of course, the next step will be to consider the analog phases in real materials. This brings in additional challenges: in the present work, we have not included the effect of scattering between electrons or electron-phonon and other defects. A phenomenological way to consider such effects is by including a dephasing time in the analysis [54]. This can help produce a cleaner spectrum by removing longer trajectories contributing to the HHG spectra. We leave this as an outlook. In addition, the role of the many-body electron-electron interaction has been assumed to be negligible and this has not been considered in this work.

Finally, as an outlook, we would like to point out that proposed HHG spectroscopy can serve as a tool for topological

phase detection in 2D topological superconductors classified by an integer-valued Chern number. In topological superconductors, the nontrivial topology is related to the quantization of electronic Hall thermal conductance [55–57]. However, thermal conductance measurements have not reached the required sophistication to observe the quantization and recently only machine learning approaches to topological invariants' detection [58] were proposed. As such, HHG spectroscopy is a promising tool for Chern number identification in topological superconductors.

#### ACKNOWLEDGMENTS

ICFO group acknowledges support from: ERC AdG NOQIA; MCIN/AEI (PGC2018-0910.13039/501100011033, CEX2019-000910-S/10.13039/501100011033, Plan National FIDEUA PID2019-106901GB-I00, Plan National STAMEENA PID2022-139099NB-I00 project funded by MCIN/AEI/10.13039/501100011033 and by the “European Union NextGenerationEU/PRTR” (PRTR-C17.I1), FPI); QUANTERA MAQS PCI2019-111828-2); QUANTERA DYNAMITE PCI2022-132919 (QuantERA II Programme co-funded by European Union's Horizon 2020 program under Grant Agreement No 101017733), Ministry of Economic Affairs and Digital Transformation of the Spanish Government through the QUANTUM ENIA project call–Quantum Spain project, and by the European Union through the Recovery, Transformation, and Resilience Plan NextGenerationEU within the framework of the Digital Spain 2026 Agenda; Fundació Cellex; Fundació Mir-Puig; Generalitat de Catalunya (European Social Fund FEDER

and CERCA program, AGAUR Grant No. 2021 SGR 01452, QuantumCAT U16-011424, co-funded by ERDF Operational Program of Catalonia 2014-2020); Barcelona Supercomputing Center MareNostrum (FI-2023-1-0013); EU Quantum Flagship (PASQuanS2.1, 101113690); EU Horizon 2020 FET-OPEN OPTologic (Grant No 899794); EU Horizon Europe Program (Grant Agreement 101080086–NeQST), ICFO Internal “QuantumGaudi” project; European Union's Horizon 2020 program under the Marie Skłodowska-Curie grant agreement No 847648; “La Caixa” Junior Leaders fellowships, La Caixa” Foundation (ID 100010434): CF/BQ/PR23/11980043. U.B. acknowledges the project that gave rise to these results, received the support of a fellowship (funded from the European Union's Horizon 2020 research and innovation programme under the Marie Skłodowska-Curie grant agreement No 847648) from “la Caixa” Foundation (ID 100010434). The fellowship codes “LCF/BQ/PR23/11980043”. M.L.B. acknowledges the financial support from MCIN/AEI/10.13039/501100011033. M.M.M. and M.D. acknowledge support from the National Science Centre (Poland) under Grant No. DEC-2018/29/B/ST3/01892. M.P. acknowledges the support of the Polish National Agency for Academic Exchange, the Bekker programme no: PPN/BEK/2020/1/00317. Views and opinions expressed are, however, those of the author(s) only and do not necessarily reflect those of the European Union, European Commission, European Climate, Infrastructure and Environment Executive Agency (CINEA), nor any other granting authority. Neither the European Union nor any granting authority can be held responsible for them.

- 
- [1] M. Z. Hasan and C. L. Kane, Colloquium: Topological insulators, *Rev. Mod. Phys.* **82**, 3045 (2010).
- [2] J. K. Asbóth, L. Oroszlány, and A. Pályi, A short course on topological insulators: Band-structure topology and edge states in one and two dimensions, *Lect. Notes Phys.* **919**, 166 (2016).
- [3] M. Jangjan and M. V. Hosseini, Floquet engineering of topological metal states and hybridization of edge states with bulk states in dimerized two-leg ladders, *Sci. Rep.* **10**, 14256 (2020).
- [4] M. Jangjan and M. V. Hosseini, Topological phase transition between a normal insulator and a topological metal state in a quasi-one-dimensional system, *Sci. Rep.* **11**, 12966 (2021).
- [5] M. Jangjan and M. V. Hosseini, Topological properties of subsystem-symmetry-protected edge states in an extended quasi-one-dimensional dimerized lattice, *Phys. Rev. B* **106**, 205111 (2022).
- [6] X.-L. Qi and S.-C. Zhang, Topological insulators and superconductors, *Rev. Mod. Phys.* **83**, 1057 (2011).
- [7] O. Viyuela, A. Rivas, S. Gasparinetti, A. Wallraff, S. Filipp, and M. A. Martín-Delgado, Observation of topological Uhlmann phases with superconducting qubits, *npj Quantum Inf.* **4**, 10 (2018).
- [8] M. Atala, M. Aidelsburger, J. T. Barreiro, D. Abanin, T. Kitagawa, E. Demler, and I. Bloch, Direct measurement of the Zak phase in topological Bloch bands, *Nat. Phys.* **9**, 795 (2013).
- [9] M. C. Rechtsman, J. M. Zeuner, Y. Plotnik, Y. Lumer, D. Podolsky, F. Dreisow, S. Nolte, M. Segev, and A. Szameit, Photonic Floquet topological insulators, *Nature (London)* **496**, 196 (2013).
- [10] S. Stützer, Y. Plotnik, Y. Lumer, P. Titum, N. H. Lindner, M. Segev, M. C. Rechtsman, and A. Szameit, Photonic topological Anderson insulators, *Nature (London)* **560**, 461 (2018).
- [11] J. Ningyuan, C. Owens, A. Sommer, D. Schuster, and J. Simon, Time- and site-resolved dynamics in a topological circuit, *Phys. Rev. X* **5**, 021031 (2015).
- [12] A. Yu. Kitaev, Fault-tolerant quantum computation by anyons, *Ann. Phys. (NY)* **303**, 2 (2003).
- [13] S. Plugge, A. Rasmussen, R. Egger, and K. Flensberg, Majorana box qubits, *New J. Phys.* **19**, 012001 (2017).
- [14] L. Li, C. Yang, and S. Chen, Winding numbers of phase transition points for one-dimensional topological systems, *Europhys. Lett.* **112**, 10004 (2015).
- [15] L. Li, Z. Xu, and S. Chen, Topological phases of generalized Su-Schrieffer-Heeger models, *Phys. Rev. B* **89**, 085111 (2014).
- [16] M. Cinchetti, Topology communicates, *Nat. Nanotechnol.* **9**, 965 (2014).
- [17] N. Nagaosa and Y. Tokura, Topological properties and dynamics of magnetic skyrmions, *Nat. Nanotechnol.* **8**, 899 (2013).
- [18] H. W. Streitwolf, Physical properties of polyacetylene, *Phys. Status Solidi B* **127**, 11 (1985).



- [19] S. Block and H. W. Streitwolf, Calculated photoinduced dynamics in trans-polyacetylene, *Synth. Met.* **76**, 31 (1996).
- [20] B. Hetényi, Y. Pulcu, and S. Doğan, Calculating the polarization in bipartite lattice models: Application to an extended Su-Schrieffer-Heeger model, *Phys. Rev. B* **103**, 075117 (2021).
- [21] B. Pérez-González, M. Bello, Á. Gómez-León, and G. Platero, Interplay between long-range hopping and disorder in topological systems, *Phys. Rev. B* **99**, 035146 (2019).
- [22] P. Delplace, D. Ullmo, and G. Montambaux, Zak phase and the existence of edge states in graphene, *Phys. Rev. B* **84**, 195452 (2011).
- [23] X. Li, E. Zhao, and W. V. Liu, Topological states in a ladder-like optical lattice containing ultracold atoms in higher orbital bands, *Nat. Commun.* **4**, 1523 (2013).
- [24] S. Ganeshan, K. Sun, and S. Das Sarma, Topological zero-energy modes in gapless commensurate Aubry-André-Harper models, *Phys. Rev. Lett.* **110**, 180403 (2013).
- [25] D. Xie, W. Gou, T. Xiao, B. Gadway, and B. Yan, Topological characterizations of an extended Su-Schrieffer-Heeger model, *npj Quantum Inf.* **5**, 55 (2019).
- [26] F. Krausz and M. Ivanov, Attosecond physics, *Rev. Mod. Phys.* **81**, 163 (2009).
- [27] F. Calegari, G. Sansone, S. Stagira, C. Vozzi, and M. Nisoli, Advances in attosecond science, *J. Phys. B: At. Mol. Opt. Phys.* **49**, 062001 (2016).
- [28] H. K. Keldar, V. Apalkov, and M. I. Stockman, Graphene superlattices in strong circularly polarized fields: Chirality, Berry phase, and attosecond dynamics, *Phys. Rev. B* **96**, 075409 (2017).
- [29] D. Bauer and K. K. Hansen, High-harmonic generation in solids with and without topological edge states, *Phys. Rev. Lett.* **120**, 177401 (2018).
- [30] C. Jürß and D. Bauer, High-harmonic generation in Su-Schrieffer-Heeger chains, *Phys. Rev. B* **99**, 195428 (2019).
- [31] R. Silva, Á. Jiménez-Galán, B. Amorim, O. Smirnova, and M. Ivanov, Topological strong-field physics on sub-laser-cycle timescale, *Nat. Photon.* **13**, 849 (2019).
- [32] A. Chacón, D. Kim, W. Zhu, S. P. Kelly, A. Dauphin, E. Pisanty, A. S. Maxwell, A. Picón, M. F. Ciappina, D. E. Kim, C. Ticknor, A. Saxena, and M. Lewenstein, Circular dichroism in higher-order harmonic generation: Heralding topological phases and transitions in Chern insulators, *Phys. Rev. B* **102**, 134115 (2020).
- [33] H. Druke and D. Bauer, Robustness of topologically sensitive harmonic generation in laser-driven linear chains, *Phys. Rev. A* **99**, 053402 (2019).
- [34] T. N. Ikeda, K. Chinzei, and H. Tsunetsugu, Floquet-theoretical formulation and analysis of high-order harmonic generation in solids, *Phys. Rev. A* **98**, 063426 (2018).
- [35] A. Pattanayak, S. Pujari, and G. Dixit, Role of majorana fermions in high-harmonic generation from Kitaev chain, *Sci. Rep.* **12**, 6722 (2022).
- [36] N. Baldelli, U. Bhattacharya, D. González-Cuadra, M. Lewenstein, and T. Graß, Detecting Majorana zero modes via strong field dynamics, *ACS Omega* **7**, 47424 (2022).
- [37] T. T. Luu and H. J. Wörner, Measurement of the Berry curvature of solids using high-harmonic spectroscopy, *Nat. Commun.* **9**, 916 (2018).
- [38] J. Reimann, S. Schlauderer, C. P. Schmid, F. Langer, S. Baierl, K. A. Kokh, O. E. Tereshchenko, A. Kimura, C. Lange, J. Güttele *et al.*, Subcycle observation of lightwave-driven Dirac currents in a topological surface band, *Nature (London)* **562**, 396 (2018).
- [39] O. Neufeld, N. Tancogne-Dejean, H. Hübener, U. De Giovannini, and A. Rubio, Are there universal signatures of topological phases in high-harmonic generation? Probably not, *Phys. Rev. X* **13**, 031011 (2023).
- [40] R. K. Malla, D. Kim, D. E. Kim, A. Chacón, and W. J. M. Kort-Kamp, Ultrafast nonequilibrium dynamics and high-harmonic generation in two-dimensional quantum spin Hall materials, *Phys. Rev. Mater.* **7**, L051201 (2023).
- [41] S. de Vega, J. D. Cox, F. Sols, and F. J. Garcia de Abajo, Strong-field-driven dynamics and high-harmonic generation in interacting one dimensional systems, *Phys. Rev. Res.* **2**, 013313 (2020).
- [42] W. P. Su, J. R. Schrieffer, and A. J. Heeger, Solitons in polyacetylene, *Phys. Rev. Lett.* **42**, 1698 (1979).
- [43] E. J. Meier, F. A. An, and B. Gadway, Observation of the topological soliton state in the Su-Schrieffer-Heeger model, *Nat. Commun.* **7**, 13986 (2016).
- [44] R. K. Malakar and A. K. Ghosh, Engineering topological phases of any winding and Chern numbers in extended Su-Schrieffer-Heeger models, *J. Phys.: Condens. Matter* **35**, 335401 (2023).
- [45] V. Lienhard, S. de Léséleuc, P. Scholl, D. Barredo, T. Lahaye, and A. Browaeys, Experimental realization of a bosonic version of the Su-Schrieffer-Heeger (SSH) model with Rydberg atoms, in *Quantum Information and Measurement (QIM) V: Quantum Technologies* (OSA, Washington, DC, 2019).
- [46] L. Thatcher, P. Fairfield, L. Merlo-Ramírez, and J. M. Merlo, Experimental observation of topological phase transitions in a mechanical 1D-SSH model, *Phys. Scr.* **97**, 035702 (2022).
- [47] S. K. Kanungo, J. D. Whalen, Y. Lu, M. Yuan, S. Dasgupta, F. B. Dunning, K. R. A. Hazzard, and T. C. Killian, Realizing topological edge states with Rydberg-atom synthetic dimensions, *Nat. Commun.* **13**, 972 (2022).
- [48] T. G. Rappoport, Y. V. Bludov, F. H. L. Koppens, and N. M. R. Peres, Topological graphene plasmons in a plasmonic realization of the Su-Schrieffer-Heeger model, *ACS Photon.* **8**, 1817 (2021).
- [49] A. D. Bandrauk, S. Chelkowski, D. J. Diestler, J. Manz, and K.-J. Yuan, Quantum simulation of high-order harmonic spectra of the hydrogen atom, *Phys. Rev. A* **79**, 023403 (2009).
- [50] J. C. Baggesen and L. B. Madsen, On the dipole, velocity and acceleration forms in high-order harmonic generation from a single atom or molecule, *J. Phys. B: At. Mol. Opt. Phys.* **44**, 115601 (2011).
- [51] B. Sundaram and P. W. Milonni, High-order harmonic generation: Simplified model and relevance of single-atom theories to experiment, *Phys. Rev. A* **41**, 6571 (1990).
- [52] P. Podder, T. Z. Khan, M. H. Khan, and M. M. Rahman, Comparative performance analysis of hamming, hanning and blackman window, *Int. J. Comput. Appl.* **96**, 1 (2014).
- [53] D. Moos, C. Jürß, and D. Bauer, Intense-laser-driven electron dynamics and high-order harmonic generation in solids including topological effects, *Phys. Rev. A* **102**, 053112 (2020).
- [54] J. Alcalá, U. Bhattacharya, J. Biegert, M. Ciappina, U. Elu, T. Graß, P. T. Grochowski, M. Lewenstein, A. Palau,

- T. P. H. Sidiropoulos, T. Steinle, and I. Tyulnev, High-harmonic spectroscopy of quantum phase transitions in a high- $T_c$  superconductor, *Proc. Natl. Acad. Sci. USA* **119**, e2207766119 (2022).
- [55] M. Z. Hasan, S.-Y. Xu, and G. Bian, Topological insulators, topological superconductors and Weyl fermion semimetals: Discoveries, perspectives and outlooks, *Phys. Scr.* **2015**, 014001 (2015).
- [56] M. Sato and Y. Ando, Topological superconductors: A review, *Rep. Prog. Phys.* **80**, 076501 (2017).
- [57] M. M. Sharma, P. Sharma, N. K. Karn, and V. P. S. Awana, Comprehensive review on topological superconducting materials and interfaces, *Supercond. Sci. Technol.* **35**, 083003 (2022).
- [58] P. Baireuther, M. Płodzień, T. Ojanen, J. Tworzydło, and T. Hyart, Identifying Chern numbers of superconductors from local measurements, [arXiv:2112.06777](https://arxiv.org/abs/2112.06777).